1. Supplementary material

1.1 *Predictive process*

Figure 1 shows the knots of the predictive process used to fit the smoothed downscaler model with spatially varying random weights in our application.

[Figure 1 about here.]

1.2 *Posterior summaries for the smoothed downscaler model with spatially-varying weights*

Figure 2 presents trace plots and density estimates of the posterior marginal distribution of: τ^2, variance of the white noise process $\epsilon(\mathbf{s}, t)$, $\sigma^2_{\beta_0}$, variance of the spatio-temporal process $\beta_0(\mathbf{s}, t)$, and σ^2_Q, variance of the latent spatio-temporal process $Q(\mathbf{r}, t)$ used to define the spatially varying random weights $w_k(\mathbf{s}, t)$.

[Figure 2 about here.]

Figure 3 and Figure 4 shows trace plots and density estimates of the posterior marginal distribution of $\beta_{0,t}$ and $\beta_{1,t}$ for $t = 1, 2$, respectively.

[Figure 3 about here.]

[Figure 4 about here.]

Figure 5 shows trace plots and density estimates of the posterior marginal distribution of $Q(\mathbf{r}^\star, t)$ at sites $\mathbf{r}_1^\star$ and $\mathbf{r}_2^\star$ and time $t = 1$.

[Figure 5 about here.]

Figure 6 and Figure 7 present trace plots and density estimates of the posterior marginal distribution of $\phi_{0,t}$, decay parameter of the spatio-temporal process $\beta_0(\mathbf{s}, t)$, at times $t = 2, 4$ and $t = 5, 6$, respectively.

[Figure 6 about here.]

[Figure 7 about here.]

1.3 *Spatially-varying weights*

Figure 8 presents the posterior mean of the weights $w_k(\mathbf{s}, t)$ at the same four sites $\mathbf{s}_1$, $\mathbf{s}_2$, $\mathbf{s}_3$, $\mathbf{s}_4$ shown in the paper for the two additional days of July 20, 2001 and August 9, 2001.

[Figure 8 about here.]

1.4 *Calibration of CMAQ*

Figure 9 shows the posterior mean and the 95% credible interval for the global calibration coefficients $\beta_{0,t}$ and $\beta_{1,t}$ of the CMAQ output over the three summer months of June, July and August 2001.

[Figure 9 about here.]

1.5 *Predictive power of the new regressor $\tilde{x}(\mathbf{s}, t)$*

Figure 10 presents scatterplots of the square root of observed ozone concentration versus: (i) the square root of CMAQ output of ozone concentration; (ii) the posterior mean of the smoothed CMAQ output generated by the smoothed GMRF downscaler and (ii) the posterior mean of the smoothed CMAQ output yielded by the smoothed downscaler model with spatially varying random weights.

[Figure 10 about here.]

1.6 *Comparison of predictive performances for the three downscaler models*

Figure 11 examines more closely the difference in predictive performance for the three downscaler models site by site. More precisely, Figure 11(a) shows, for each validation site, the difference between the site-specific PMSE yielded by our earlier downscaler model and the site-specific PMSE yielded by the GMRF smoothed downscaler as a function of the average distance of the site from training monitoring sites. Similarly, Figure 11(b) presents, for each validation site, the difference between the site-specific PMSE yielded by original downscaler

model and the site-specific PMSE yielded by the smoothed downscaler with spatially varying random weights. Negative values indicate that the GMRF smoothed downscaler, respectively, the smoothed downscaler with spatially varying random weights produce predictions with greater PMSE than the earlier downscaler model, positive values indicate the opposite situation.

[Figure 11 about here.]

12 July 2011.

Knots of the predictive process
June 1 – August 31, 2001
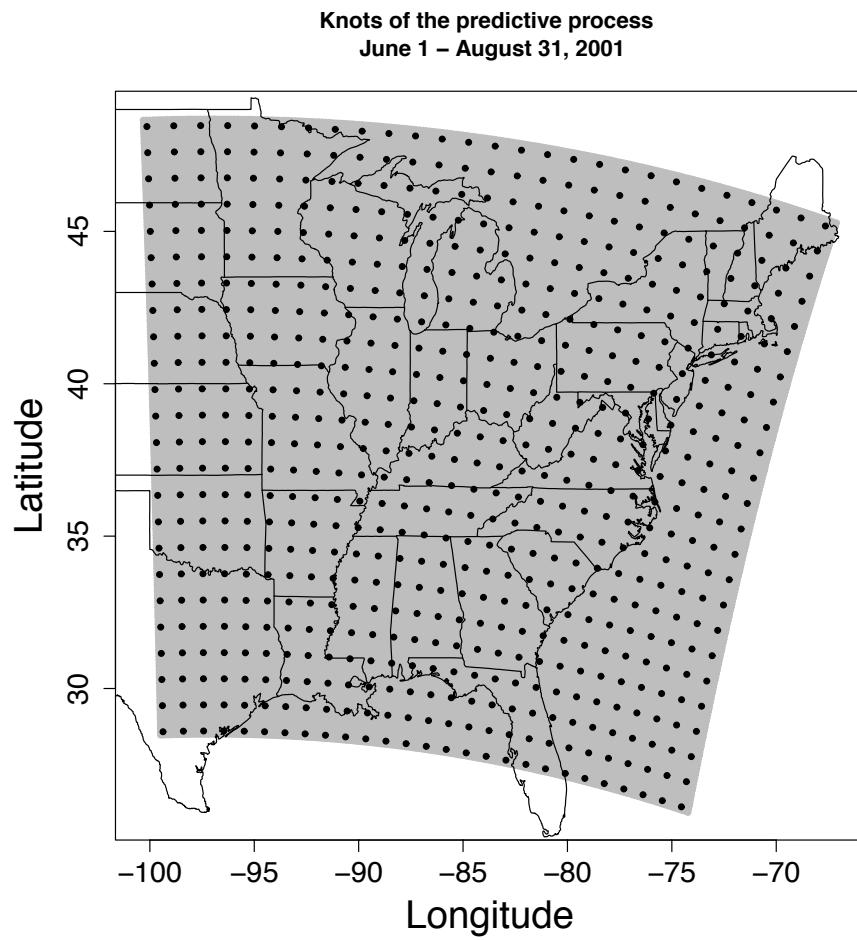
Figure 1: Knots of the predictive process.
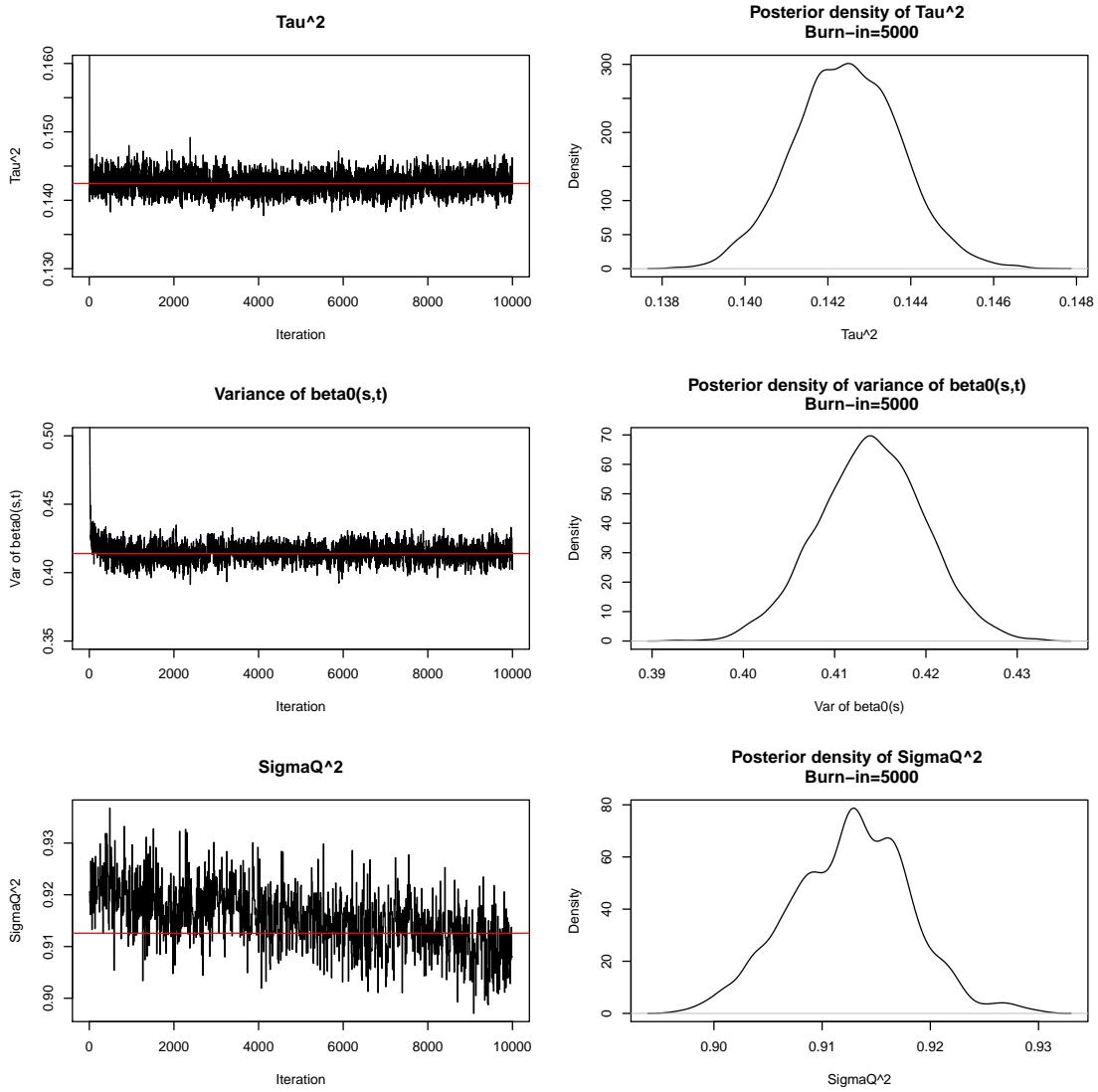
Figure 2: Trace plots and density estimates of the posterior marginal distribution of: τ^2, $\sigma^2_{\beta_0}$, and σ^2_Q.
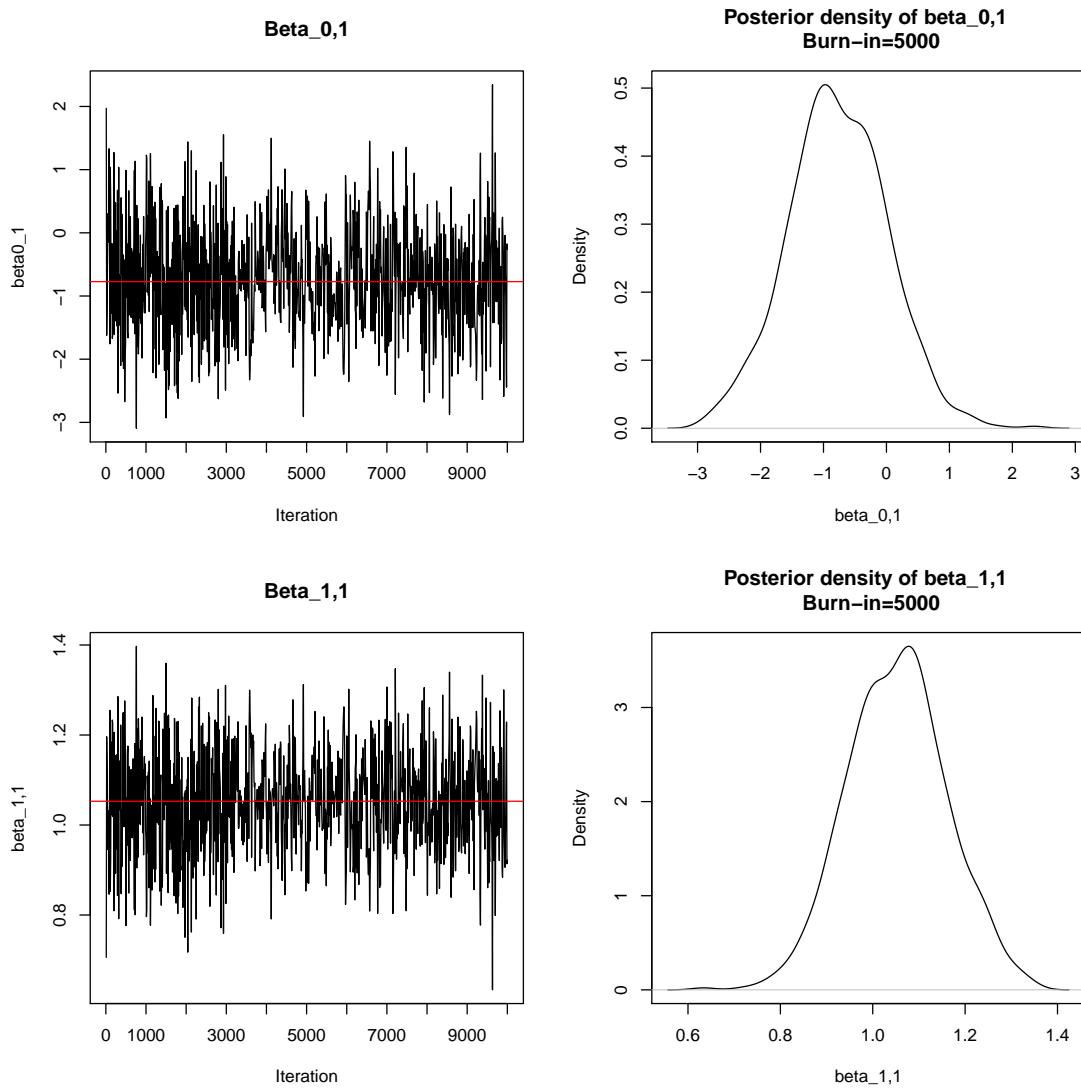
Figure 3: Trace plots and density estimates of the posterior marginal distribution of $\beta_{0,t}$ and $\beta_{1,t}$ for $t = 1$.
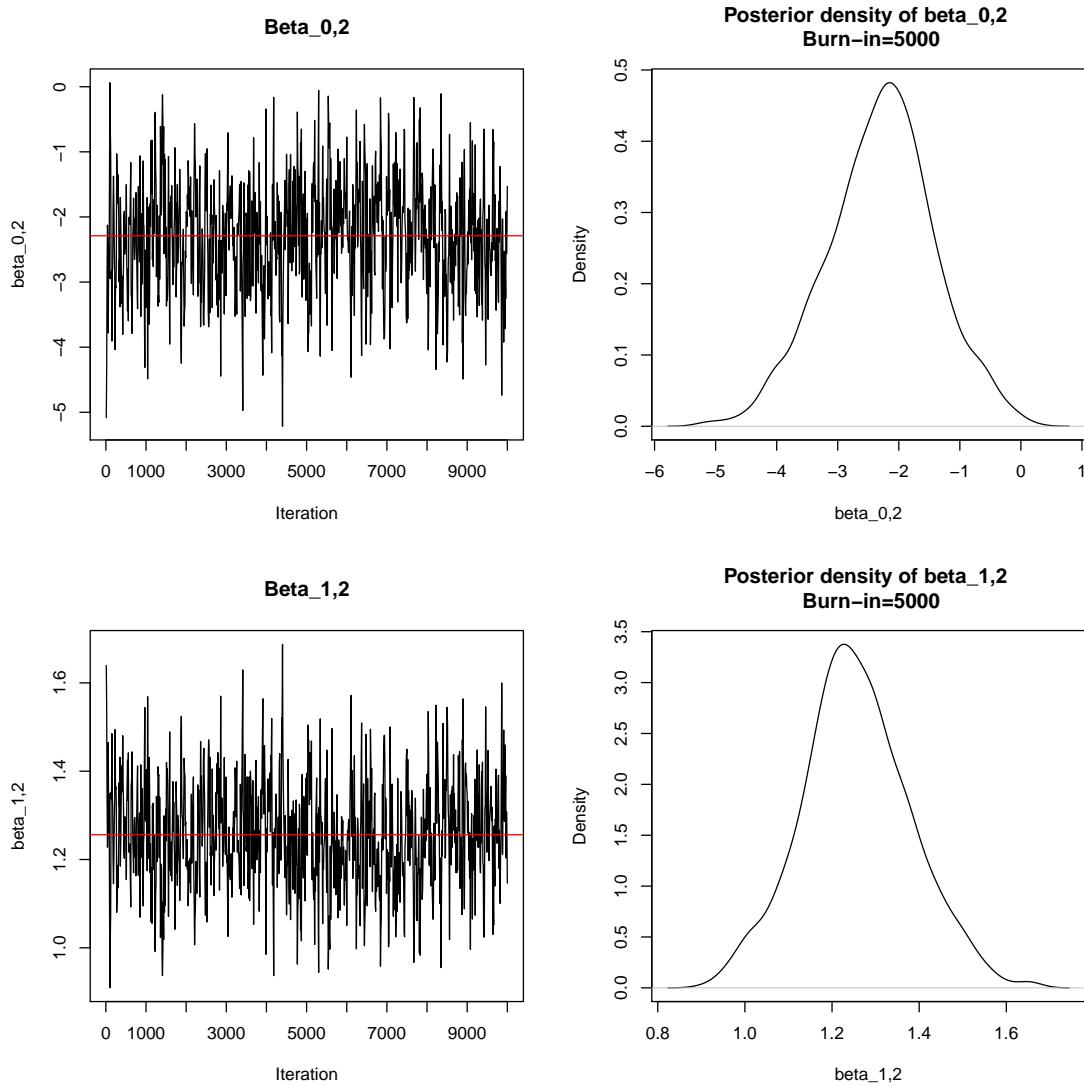
Figure 4: Trace plots and density estimates of the posterior marginal distribution of $\beta_{0,t}$ and $\beta_{1,t}$ for $t = 2$.
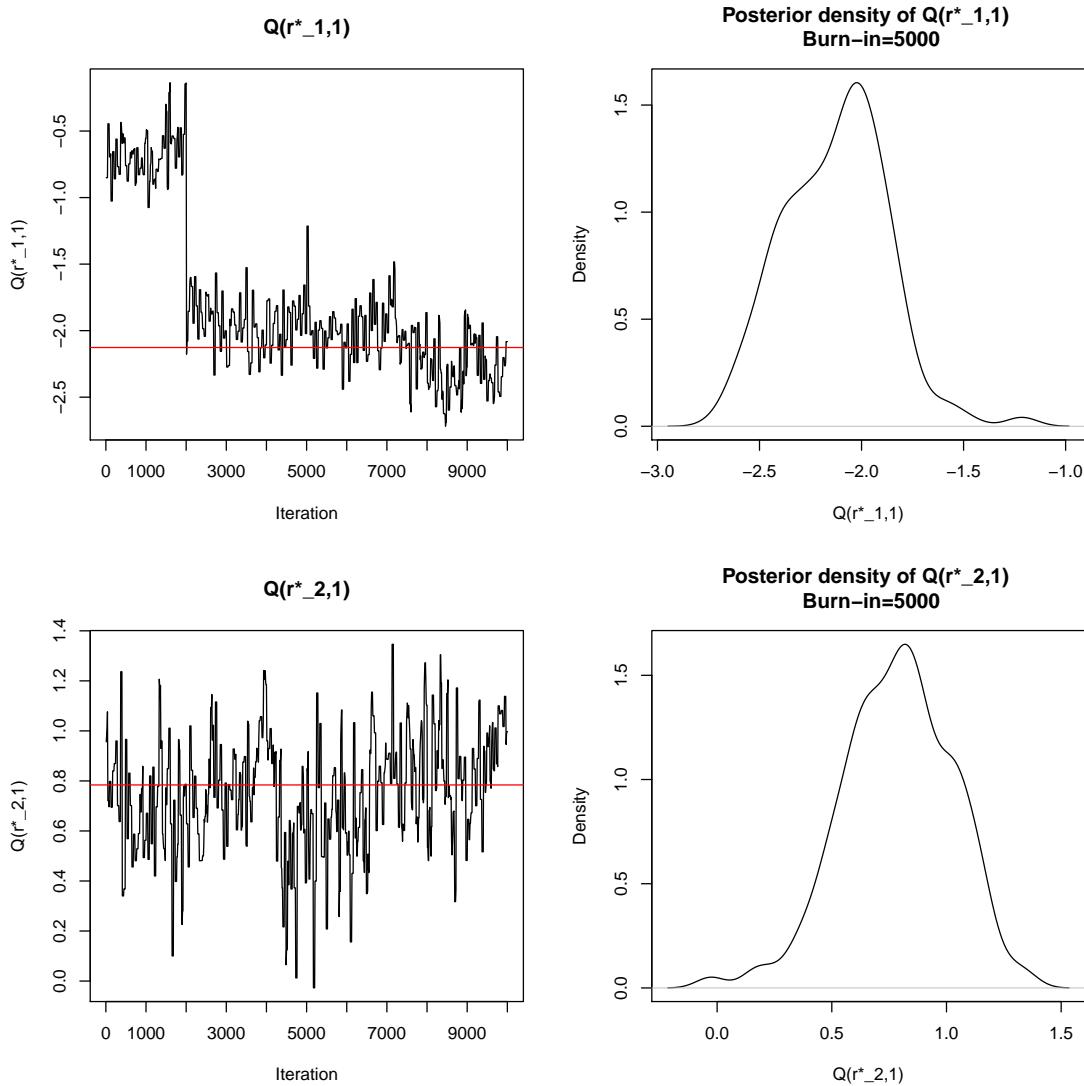
Figure 5: Trace plots and density estimates of the posterior marginal distribution of $Q(\mathbf{r}_1^\star, t)$ and $Q(\mathbf{r}_2^\star, t)$ for $t = 1$.
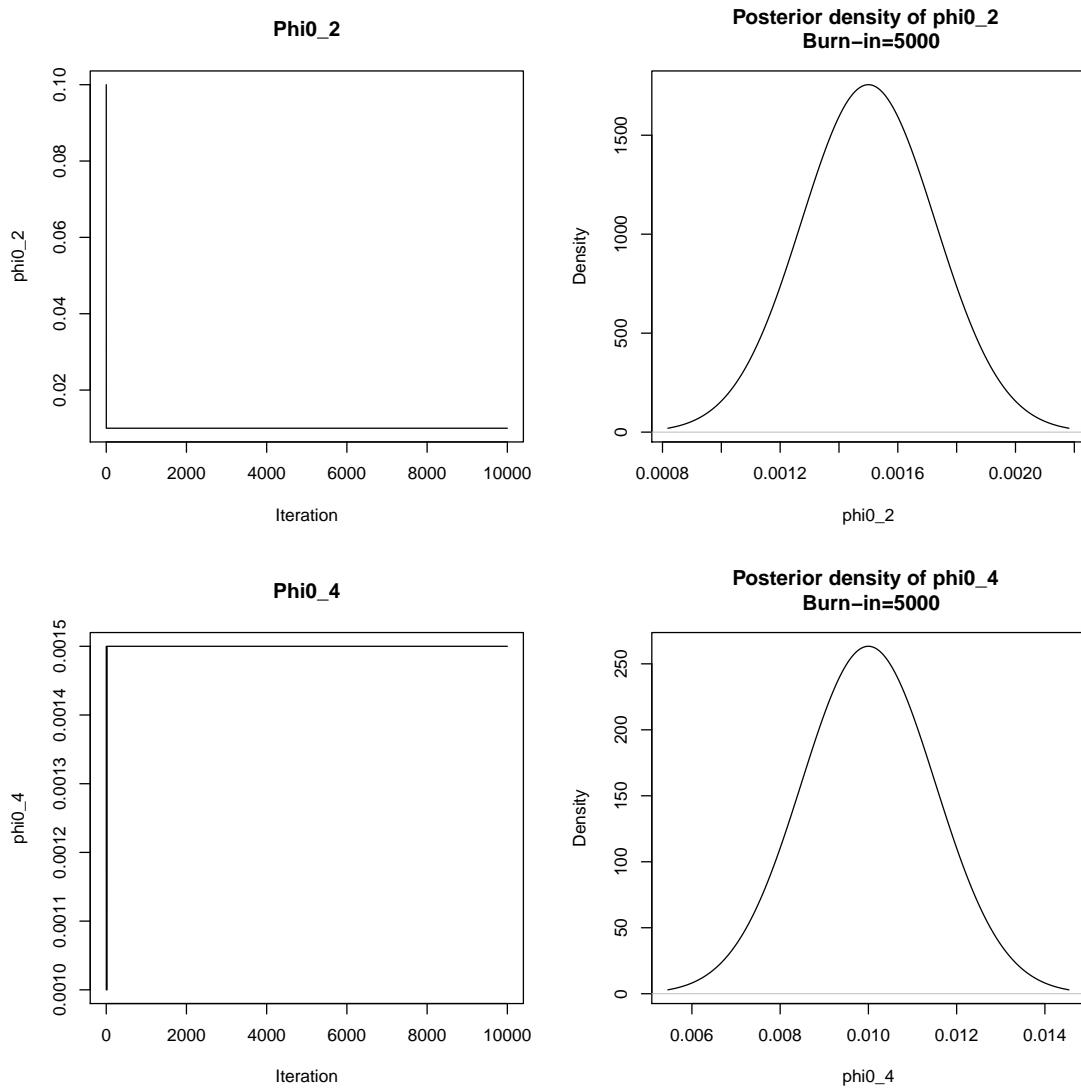
Figure 6: Trace plots and density estimates of the posterior marginal distribution of $\phi_{0,t}$ for $t = 2, 4$.
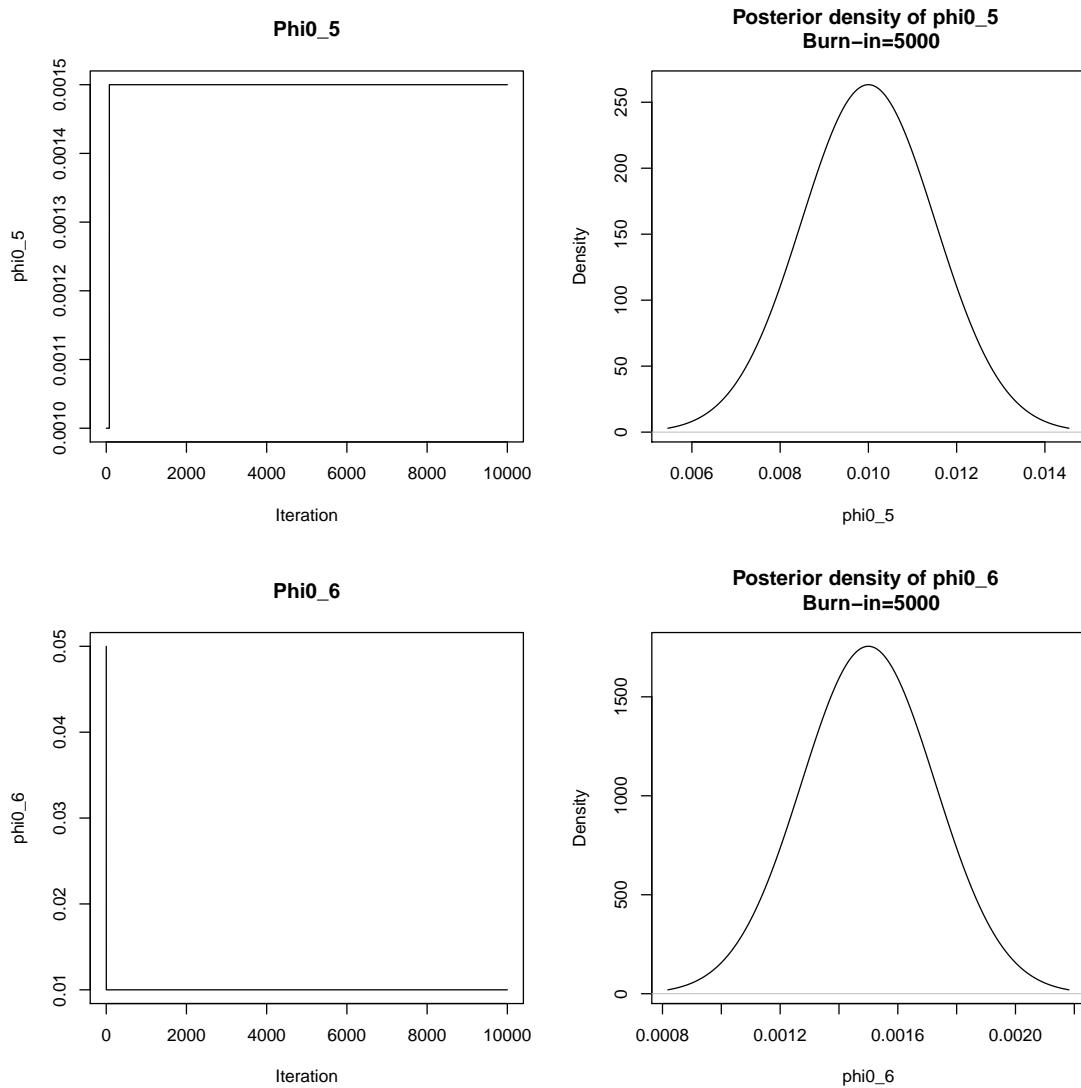
Figure 7: Trace plots and density estimates of the posterior marginal distribution of $\phi_{0,t}$ for $t = 5, 6$.
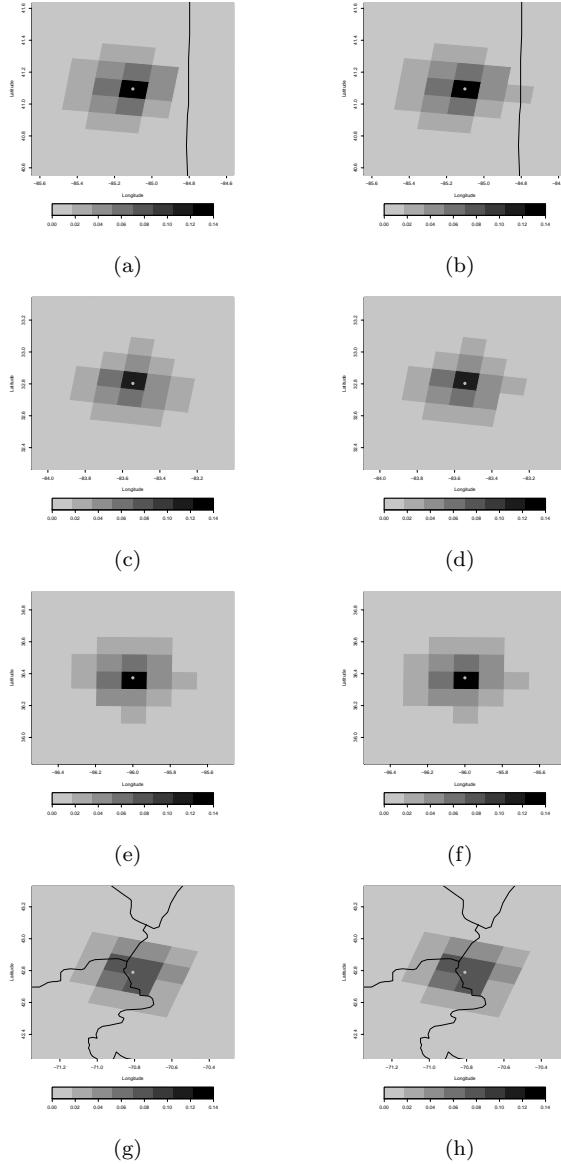
Figure 8: Posterior predictive mean of the spatially varying random weights $w_k(\mathbf{s}, t)$ for sites: (a)-(b) $\mathbf{s}_1$; (c)-(d) $\mathbf{s}_2$; (e)-(f) $\mathbf{s}_3$; and (g)-(h) $\mathbf{s}_4$ on July 20, 2001 (panels (a)-(c)-(e)-(g)) and on August 9, 2001 (panels (b)-(d)-(f)-(h)).
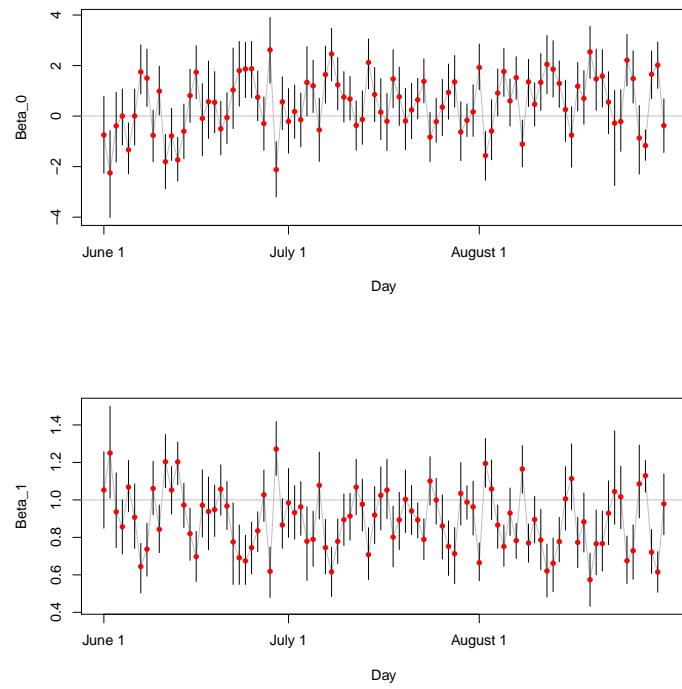
Figure 9: Posterior mean (red dots) and 95% credible intervals for $\beta_{0,t}$ and $\beta_{1,t}$ for $t = 1, \ldots, 92$.
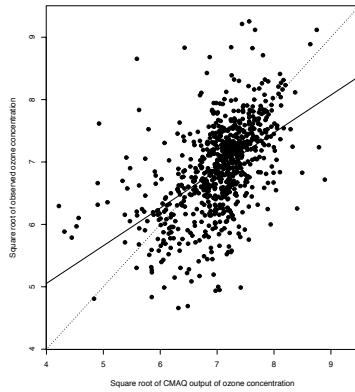
(a)
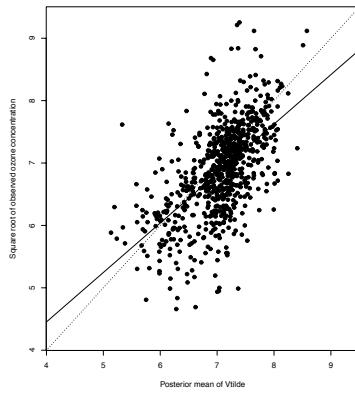
(b)
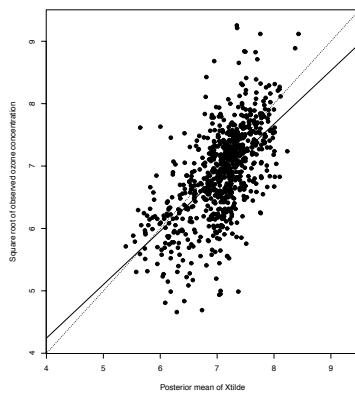
(c)

Figure 10: Scatterplot of square root of observed ozone concentration, $Y(\mathbf{s}, t)$, versus: (a) square root of CMAQ output of ozone concentration $x(B, t)$, with $\mathbf{s} \in B$, (b) posterior mean of $\tilde{V}(B, t)$, with $\mathbf{s} \in B$, and (c) posterior mean of $\tilde{x}(\mathbf{s}, t)$ for July 4, 2001 and for a subregion in the North East. In each panels, the solid and the dashed line represent, respectively, the regression line and the 45° degree line.
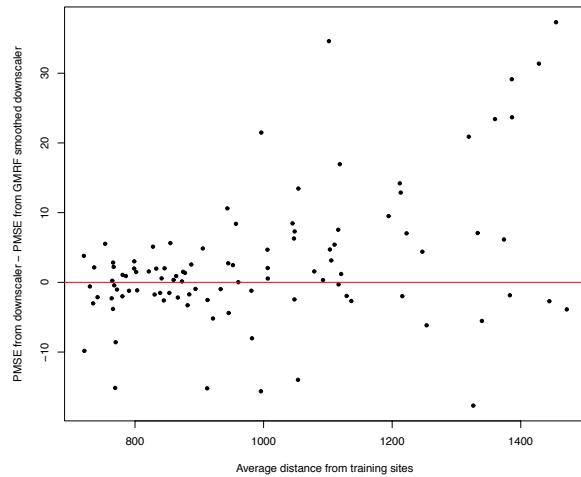
(a)
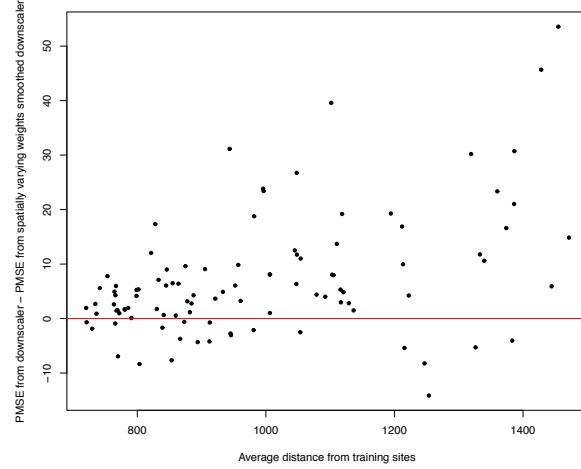
(b)

Figure 11: Plot of the difference in site-specific PMSE between (a) our earlier downscaler model and the GMRF smoothed downscaler and (b) our earlier downscaler model and the smoothed downscaler with spatially varying random weights, as a function of the average distance between the validation site and the training monitoring sites.